The Hydrometeor Classification Algorithm for the Polarimetric WSR-88D: Description and Application to an MCS

HYANGSUK PARK

Department of Astronomy and Atmospheric Sciences, Kyungpook National University, Daegu, South Korea

A. V. RYZHKOV

Cooperative Institute for Mesoscale Meteorological Studies, University of Oklahoma, and NOAA/OAR National Severe Storms Laboratory, Norman, Oklahoma

D. S. ZRNIĆ

National Severe Storms Laboratory, Norman, Oklahoma

KYUNG-EAK KIM

Department of Astronomy and Atmospheric Sciences, Kyungpook National University, Daegu, South Korea

(Manuscript received 25 August 2008, in final form 24 November 2008)

ABSTRACT

This paper contains a description of the most recent version of the hydrometeor classification algorithm for polarimetric Weather Surveillance Radar-1988 Doppler (WSR-88D). This version contains several modifications and refinements of the previous echo classification algorithm based on the principles of fuzzy logic. These modifications include the estimation of confidence factors that characterize the possible impacts of all error sources on radar measurements, the assignment of the matrix of weights that characterizes the classification power of each variable with respect to every class of radar echo, and the implementation of a class designation system based on the distance from the radar and the parameters of the melting layer that are determined as functions of azimuth with polarimetric radar measurements. These additions provide considerable flexibility and improve the discrimination between liquid and frozen hydrometeors. The new classification scheme utilizes all available polarimetric variables and discerns 10 different classes of radar echoes. Furthermore, a methodology for the new fuzzy logic classification scheme is discussed and the results are illustrated using polarimetric radar data collected with the Norman, Oklahoma (KOUN), WSR-88D prototype radar during a mesoscale convective system event on 13 May 2005.

1. Introduction

Dual-polarization radar is a unique instrument for the classification of radar echoes. Having dual-polarization capability is essential for discriminating between meteorological and nonmeteorological scatterers and for distinguishing between different hydrometeor types, such as rain, hail, graupel, and snow of different habits. Furthermore, knowledge of the hydrometeor type within the radar resolution volume is required for choosing an appropriate polarimetric rain rate relation to accurately quantify the amount of precipitation (Giangrande and Ryzhkov 2008).

Principles of fuzzy logic form the basis for most polarimetric classification algorithms; these were first explored by Straka and Zrnić (1993) and Straka (1996) and have since been further refined into more sophisticated classification routines described by Zrnić and Ryzhkov (1999), Vivekanandan et al. (1999), Liu and Chandrasekar (2000), Zrnić et al. (2001), Schuur et al. (2003), Keenan (2003), Lim et al. (2005), and Marzano et al. (2008), among others.

The hydrometeor classification capability of a polarimetric prototype of the Weather Surveillance Radar-1988

Corresponding author address: Alexander V. Ryzhkov, CIMMS/NSSL, 120 David Boren Dr., Norman, OK 73072.
E-mail: alexander.ryzhkov@noaa.gov

DOI: 10.1175/2008WAF2222205.1

© 2009 American Meteorological Society

Doppler (WSR-88D) in an operational environment was tested in Oklahoma in 2002–03 during a demonstration project called the Joint Polarization Experiment (JPOLE; Ryzhkov et al. 2005b). Such a capability, together with other polarization products, was very well received by the National Weather Service (NWS) forecasters during this operational demonstration (Scharfenberg et al. 2005). One of the first versions of the National Severe Storms Laboratory (NSSL) hydrometeor classification algorithm (HCA) demonstrated a remarkable level of skill in detecting hail, which was verified during the JPOLE campaign (Heinselman and Ryzhkov 2006). Nonetheless, further validation studies revealed several problems with early versions of HCA that had to be addressed. These problems are also inherent in other classification routines that are utilized elsewhere.

First, it was found that the quality of the classification depends on the quality of the polarimetric radar measurements. It became evident that radar estimates with enhanced measurement errors should be given lower weight in the classification scheme. Second, due to antenna beam broadening at longer distances, the radar resolution volume may contain liquid, frozen, and mixed-phase particles, and hence certain rules for class designation should be formulated based on the size of the sampling volume as well as on the height and depth of the melting layer. Finally, discrimination between convective and stratiform precipitation types is necessary to facilitate better distinction between dry–wet graupel and dry–wet snow for which the polarimetric variables overlap and hence may not be well separated.

Since JPOLE, the NSSL HCA scheme was modified by incorporating additional routines that account for possible errors in radar measurements, beam broadening, the relative location of the radar sampling volume with respect to the melting layer (ML), and the nature of the precipitation (i.e., convective versus stratiform). The objectives of this paper are to describe the most recent version of the HCA, which was recommended by the U.S. National Weather Service for initial deployment on the network of polarimetrically upgraded WSR-88Ds, and to illustrate its performance in the case of a mesoscale convective system (MCS) observed in central Oklahoma on 13 May 2005.

The content of the paper is as follows. After the introduction, the general structure of the algorithm is described in section 2 where the classes of radar echoes are also listed and the details of the aggregate computation are given. Section 3 introduces the confidence vector, which depends on the statistical and physical parameters affecting the measurements. Constraints on the allowed classes are imposed using the distance from the radar, beamwidth, and parameters of the melting layer as discussed in section 4. The case study is presented in section 5, which is followed by a summary and conclusions in section 6.

2. General structure of the algorithm

a. Echo classes and radar variables

The HCA discriminates between 10 classes of radar echo: 1) ground clutter, including that due to anomalous propagation (GC/AP); 2) biological scatterers (BS); 3) dry aggregated snow (DS); 4) wet snow (WS); 5) crystals of various orientations (CR); 6) graupel (GR); 7) "big drops" (BD); 8) light and moderate rain (RA); 9) heavy rain (HR); and 10) a mixture of rain and hail (RH). The big-drops category designates rain with a drop size distribution skewed toward large raindrops. This usually implies the presence of drops bigger than 3 mm and the deficit of smaller drops. Big drop signatures are generally due to size sorting associated with either convective updrafts often exemplified with Z_{DR} columns (Wakimoto and Bringi 1988) or wind shear and veering, which cause Z_{DR} "arcs" (Kumjian and Ryzhkov 2008). Both signatures have important prognostic value because the Z_{DR} columns are common in the initial stages of convective development (Bringi and Chandrasekar 2001) and Z_{DR} arcs characterize storm-relative helicity in supercell storms (Kumjian and Ryzhkov 2008). The class of biological scatterers includes insects, birds, and bats. Other nonmeteorological scatterers in the atmosphere such as tornadic debris or military chaff may fall in the category of either GC/AP or BS.

Six radar variables are directly utilized for discrimination. These are 1) the radar reflectivity factor at horizontal polarization Z, 2) the differential reflectivity Z_{DR}, 3) the cross-correlation coefficient ρ_{hv} between horizontally and vertically polarized radar returns, 4) the specific differential phase K_{DP}, 5) a texture parameter SD(Z) of the Z field, and 6) a texture parameter SD(Φ_{DP}) of the field of differential phase Φ_{DP}. The parameters SD(Z) and SD(Φ_{DP}) characterize the magnitude of the small-scale fluctuations of Z and Φ_{DP} along the radial. The estimate of SD(Z) is obtained by averaging Z data along the radial using a 1-km running-average window (i.e., four data points spaced 0.25 km apart are averaged), subtracting the smoothed estimates of Z from the original values, and calculating the root-mean-square (RMS) value of the residuals. Here, SD(Φ_{DP}) is calculated in a similar manner, but because Φ_{DP} has inherently large fluctuations, a 2-km running average is utilized. In addition to the polarimetric variables, the mean Doppler velocity V is utilized for discrimination between hail and GC/AP, although it is not

included in the set of input variables for the fuzzy logic classifier.

Due to the parameter range of K_{DP} it is more convenient to use its values in logarithmic scale rather than in linear scale. Hence, instead of K_{DP} in degrees per kilometer, we introduce the parameter LKdp, which is determined as follows:

$$\begin{aligned} \mathrm{LKdp} &= 10\log(K_{DP}) \quad \text{if} \quad K_{DP} > 10^{-3}\ {}^\circ\mathrm{km}^{-1} \\ \mathrm{LKdp} &= -30 \quad \text{if} \quad K_{DP} \le 10^{-3}\ {}^\circ\mathrm{km}^{-1}. \end{aligned} \tag{1}$$

Before applying the classification procedure, Z, Z_{DR}, and ρ_{hv} are smoothed along each radial using a 1-km averaging window for Z and a 2-km window for Z_{DR} and ρ_{hv}. In addition, a signal-to-noise ratio (SNR) at horizontal polarization and a ratio of noise powers in the two orthogonal channels are used for noise correction of Z_{DR} and ρ_{hv} (Schuur et al. 2003). Two smoothed radial profiles of Φ_{DP} are obtained by editing and using two averaging windows corresponding to nine consecutive samples in the case of "lightly filtering" (2-km window width if the sample spacing is 0.25 km) and 25 successive samples for "heavily filtering" (6-km window width). Both Z and Z_{DR} are corrected for attenuation in precipitation using heavily filtered Φ_{DP} by adding the estimated biases

$$\begin{aligned} \Delta Z^{\mathrm{att}}(\mathrm{dB}) &= 0.04\Phi_{DP}(^\circ) \quad \text{and} \\ \Delta Z_{DR}^{\mathrm{att}}(\mathrm{dB}) &= 0.004\Phi_{DP}(^\circ) \end{aligned} \tag{2}$$

to the measured values of Z and Z_{DR} (Ryzhkov and Zrnić 1995).

Finally, two estimates of K_{DP} are obtained from a slope of a least squares fit of the filtered Φ_{DP} using two range intervals corresponding to 9 and 25 consecutive range gates. A lightly filtered K_{DP} is used for classification if $Z > 40$ dBZ and a heavily filtered K_{DP} is selected otherwise (Ryzhkov and Zrnić 1996).

b. Computation of aggregation values

The classification scheme presented here combines the information content of the polarimetric variables. This is done by assigning a typical range of values for the various polarimetric variables to each class of radar echo. Each range of values is quantified with a membership (weighting) function. Membership functions are summed, or multiplied, or otherwise combined for each class in a process called aggregation. The aggregated value of a class characterizes the likelihood that this particular class is associated with the values of variables measured by the radar. An aggregation value A_i for the ith class of radar echoes is defined here as

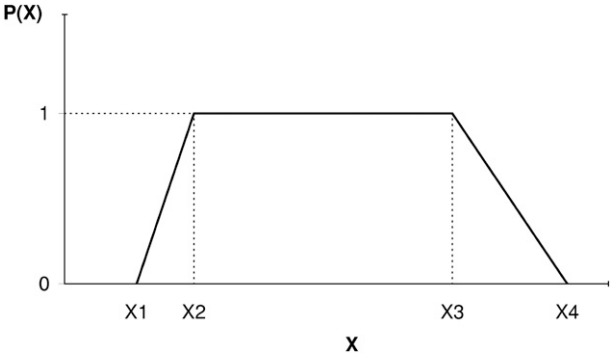

FIG. 1. Trapezoidal membership function, where X is an arbitrary polarimetric variable.

$$A_i = \frac{\sum_{j=1}^{6} W_{ij}\, Q_j\, P^{(i)}(V_j)}{\sum_{j=1}^{6} W_{ij}\, Q_j}, \tag{3}$$

where $P^{(i)}(V_j)$ is a membership function (which characterizes the distribution of the jth variable for the ith class), W_{ij} is a weight between 0 and 1 assigned to the ith class and the jth variable, and Q_j is an element of the confidence vector assigned to the jth variable. The classification decision is based on the maximal aggregation value.

Note that in the HCA we use an additive aggregation routine that implies a summation of inputs from different variables with certain weights. Other investigators have used multiplication or the combination of addition and multiplication (e.g., Liu and Chandrasekar 2000; Lim et al. 2005). Early versions of the HCA (Zrnić et al. 2001; Schuur et al. 2003) employed "hybrid" aggregation schemes in which the membership functions of Z_{DR} and K_{DP} were constructed as products of $P^{(i)}(Z)$ and conditional functions $P_Z^{(i)}(Z_{DR})$ and $P_Z^{(i)}(K_{DP})$, respectively. Our experience shows that the hybrid schemes are too vulnerable to the Z biases caused by miscalibration and/or attenuation and therefore the choice was made in favor of a simple additive aggregation procedure.

The membership functions $P^{(i)}(V_j)$ are assumed to have trapezoidal shape with a maximal value of 1 and a minimal value of 0 (Fig. 1). The trapezoidal functions are described by four parameters: x_1, x_2, x_3, and x_4. These parameters are presented in Table 1 for each of the 60 membership functions. Trapezoids adequately approximate the symmetric shapes of the probability distributions of radar variables as well as the asymmetric [such as cross-correlation coefficient ρ_{hv}; Zrnić et al. (2006)];

TABLE 1. Parameters of the membership functions for 10 classes. Reflectivity-dependent parameters f_1–f_3 and g_1–g_2 are defined by Eqs. (4) and (5), respectively.

	GC/AP	BS	DS	WS	CR	GR	BD	RA	HR	RH
					$P[Z(\mathrm{dB}Z)]$					
x_1	15	5	5	25	0	25	20	5	40	45
x_2	20	10	10	30	5	35	25	10	45	50
x_3	70	20	35	40	20	50	45	45	55	75
x_4	80	30	40	50	25	55	50	50	60	80
					$P[Z_{\mathrm{DR}}(\mathrm{dB})]$					
x_1	−4	0	−0.3	0.5	0.1	−0.3	f_2–0.3	f_1–0.3	f_1–0.3	−0.3
x_2	−2	2	0.0	1.0	0.4	0.0	f_2	f_1	f_1	0.0
x_3	1	10	0.3	2.0	3.0	f_1	f_3	f_2	f_2	f_1
x_4	2	12	0.6	3.0	3.3	$f_1 + 0.3$	$f_3 + 1.0$	$f_2 + 0.5$	$f_2 + 0.5$	$f_1 + 0.5$
					$P(\rho_{\mathrm{hv}})$					
x_1	0.5	0.3	0.95	0.88	0.95	0.90	0.92	0.95	0.92	0.85
x_2	0.6	0.5	0.98	0.92	0.98	0.97	0.95	0.97	0.95	0.90
x_3	0.9	0.8	1.00	0.95	1.00	1.00	1.00	1.00	1.00	1.00
x_4	0.95	0.83	1.01	0.985	1.01	1.01	1.01	1.01	1.01	1.01
					$P(\mathrm{LKdp})$					
x_1	−30	−30	−30	−30	−5	−30	g_1–1	g_1–1	g_1–1	−10
x_2	−25	−25	−25	−25	0	−25	g_1	g_1	g_1	−4
x_3	10	10	10	10	10	10	g_2	g_2	g_2	g_1
x_4	20	10	20	20	15	20	$g_2 + 1$	$g_2 + 1$	$g_2 + 1$	$g_1 + 1$
					$P[\mathrm{SD}(Z)(\mathrm{dB})]$					
x_1	2	1	0	0	0	0	0	0	0	0
x_2	4	2	0.5	0.5	0.5	0.5	0.5	0.5	0.5	0.5
x_3	10	4	3	3	3	3	3	3	3	3
x_4	15	7	6	6	6	6	6	6	6	6
					$P[\mathrm{SD}(\Phi_{\mathrm{DP}})(°)]$					
x_1	30	8	0	0	0	0	0	0	0	0
x_2	40	10	1	1	1	1	1	1	1	1
x_3	50	40	15	15	15	15	15	15	15	15
x_4	60	60	30	30	30	30	30	30	30	30

this is not true for some other popular membership functions like Gaussian or beta (e.g., Liu and Chandrasekar 2000; Lim et al. 2005), which are symmetric.

Parameters x_1–x_4 of the membership functions of Z_{DR} and LKdp depend on radar reflectivity for all four categories of rain (BD, RA, HR, and RH). The dependency is chosen to describe a nonrectangular region in the Z, Z_{DR} space where the typical pair of these values resides for each of the four rain categories (similar to Fig. 2a in Straka et al. 2000). Thus, functions f_1–f_3 and g_1–g_2 determine the x_1–x_4 in Table 1 and are given by

$$f_1(Z) = -0.50 + 2.50 \times 10^{-3} Z + 7.50 \times 10^{-4} Z^2,$$
$$f_2(Z) = 0.68 - 4.81 \times 10^{-2} Z + 2.92 \times 10^{-3} Z^2, \quad (4)$$
$$f_3(Z) = 1.42 + 6.67 \times 10^{-2} Z + 4.85 \times 10^{-4} Z^2,$$

and

$$g_1(Z) = -44.0 + 0.8\,Z \quad \text{and}$$
$$g_2(Z) = -22.0 + 0.5\,Z, \quad (5)$$

where the radar reflectivity Z is expressed in dBZ.

The matrix of weights **W** in (3) characterizes the discriminating efficiency of each variable with respect to a particular class. The elements of the matrix **W** are presented in Table 2. As an example, ρ_{hv} is the most important variable for the identification of biological scatterers ($W_{23} = 1.0$) followed by the texture parameters of Z and Φ_{DP} ($W_{25} = W_{26} = 0.8$), Z_{DR} ($W_{22} = 0.6$), and LKdp, which does not have any diagnostic value for biological scatterers ($W_{24} = 0$). As in Lim et al. (2005), the matrix **W** is determined subjectively and its further refinement based on objective criteria will be made in future studies. One possible criterion to accomplish this refinement is the methodology described by Park et al. (2007). This methodology takes into account the degree of overlap between the probability density functions of

TABLE 2. Matrix of weights.

Class	Variable					
	Z	Z_{DR}	ρ_{hv}	LKdp	SD(Z)	SD(Φ_{DP})
GC/AP	0.2	0.4	1.0	0.0	0.6	0.8
BS	0.4	0.6	1.0	0.0	0.8	0.8
DS	1.0	0.8	0.6	0.0	0.2	0.2
WS	0.6	0.8	1.0	0.0	0.2	0.2
CR	1.0	0.6	0.4	0.5	0.2	0.2
GR	0.8	1.0	0.4	0.0	0.2	0.2
BD	0.8	1.0	0.6	0.0	0.2	0.2
RA	1.0	0.8	0.6	0.0	0.2	0.2
HR	1.0	0.8	0.6	1.0	0.2	0.2
RH	1.0	0.8	0.6	1.0	0.2	0.2

each radar variable for different classes of radar echo. More overlapping usually means lower values of weight.

3. Confidence vector

The quality of the radar echo classification is significantly affected by the accuracy of the radar measurements, which can be biased and noisy. The impact of the measurements errors is accounted for in the aggregation rule (3) via a confidence vector **Q**. In other words, for each range gate, the jth radar variable is supplemented with its confidence index Q_j depending on its vulnerability to several factors that can compromise the quality of its measurement. These factors include 1) radar miscalibration, 2) attenuation, 3) nonuniform beam filling (NBF), 4) partial beam blockage (PBB), 5) the magnitude of ρ_{hv} (which determines the statistical errors of all polarimetric variables), and 6) receiver noise. If the quality of a certain radar variable is compromised in a particular area of the radar echo, then it would be given a lower weight in the classifier. The confidence vector is defined as

$$\begin{aligned}\mathbf{Q} &= (Q_1, Q_2, Q_3, Q_4, Q_5, Q_6)\\ &= (Q_Z, Q_{ZDR}, Q_{\rho hv}, Q_{KDP}, Q_{SDZ}, Q_{SD\Phi}),\end{aligned} \tag{6}$$

where the components Q_1–Q_6 are constructed (for convenience) as products of Gaussian functions that characterize the impact of different factors on the measurement errors. For example, a confidence index for the differential reflectivity Q_{ZDR} is defined as a product of five multipliers,

$$Q_{ZDR} = F_{att}F_{nbf}F_{rhv}F_{snr}F_{pbb}, \tag{7}$$

associated with five known sources of measurement errors in Z_{DR}: differential attenuation (F_{att}), nonuniform beam filling (F_{nbf}), the value of ρ_{hv} (F_{rhv}), the signal-to-noise ratio (F_{snr}), and partial beam blockage (F_{pbb}) (Bringi and Chandrasekar 2001; Ryzhkov 2007; Giangrande and Ryzhkov 2005).

The factor F_{att} is a Gaussian function of the measured differential phase Φ_{DP}, which is proportional to differential attenuation according to (2):

$$F_{att} = \exp\left\{-0.69\left[\frac{\Phi_{DP}}{\Phi_{DP}^{(Z)}}\right]^2\right\}. \tag{8}$$

Although Z_{DR} is corrected for differential attenuation using (2), the accuracy of such a correction inevitably degrades with increasing Φ_{DP} because of the uncertainty in the coefficient of the proportionality between ΔZ_{DR}^{att} and Φ_{DP} in (2) due to drop size distribution variations and the possible presence of melting hail (Ryzhkov et al. 2007). The right side of Eq. (8) is defined in such a way that the factor F_{att} decreases twice once Φ_{DP} reaches a threshold value $\Phi_{DP}^{(Z)}$. The threshold $\Phi_{DP}^{(Z)}$ is an adaptable parameter in the HCA, which is currently set to 250°.

Similarly, the factor F_{nbf} is defined as

$$F_{nbf} = \exp\left\{-0.69\left[\frac{\Delta Z_{DR}}{\Delta Z_{DR}^{(t)}}\right]^2\right\}, \tag{9}$$

where ΔZ_{DR} is a Z_{DR} bias due to the vertical and horizontal gradients of Z and Z_{DR} within the radar resolution volume (Ryzhkov 2007):

$$\Delta Z_{DR} = 0.02\ \Omega^2\left(\frac{dZ}{d\theta}\frac{dZ_{DR}}{d\theta} + \frac{dZ}{d\varphi}\frac{dZ_{DR}}{d\varphi}\right). \tag{10}$$

Here, $\Delta Z_{DR}^{(t)}$ is an adaptable threshold (currently 0.5 dB), and Ω is a one-way 3-dB antenna pattern width (θ and φ are the elevation and azimuth pointing angles of the antenna). It is evident from (10) that the gradients of Z and Z_{DR} should be computed prior to the estimation of ΔZ_{DR}.

In full analogy, the formulas for F_{rhv}, F_{snr}, and F_{pbb} can be written as

$$F_{rhv} = \exp\left\{-0.69\left[\frac{1-\rho_{hv}}{\Delta\rho_{hv}^{(1)}}\right]^2\right\}, \tag{11}$$

$$F_{snr} = \exp\left\{-0.69\left[\frac{\mathrm{snr}^{(Zdr)}}{\mathrm{snr}}\right]^2\right\}, \quad \text{and} \tag{12}$$

$$F_{pbb} = \exp\left[-0.69\left(\frac{\alpha}{50}\right)^2\right]. \tag{13}$$

In (11)–(13), $\Delta\rho_{hv}^{(1)} = 0.2$ and $\mathrm{snr}^{(Zdr)} = 10^{0.05}$ are thresholds for ρ_{hv} and the signal-to-noise ratio (snr; in linear

scale), and α is a degree of beam blockage (in %) that is estimated from the digital elevation map for a given azimuth and elevation.

Following a similar line of reasoning, we write formulas for all six components of the confidence vector:

$$Q_Z = \exp\left(-0.69\left\{\left[\frac{\Phi_{\mathrm{DP}}}{\Phi_{\mathrm{DP}}^{(Z)}}\right]^2 + \left[\frac{\mathrm{snr}^{(Z)}}{\mathrm{snr}}\right]^2 + \left(\frac{\alpha}{50}\right)^2\right\}\right), \tag{14}$$

$$Q_{\mathrm{ZDR}} = \exp\left(-0.69\left\{\left[\frac{\Phi_{\mathrm{DP}}}{\Phi_{\mathrm{DP}}^{(\mathrm{Zdr})}}\right]^2 + \left[\frac{\Delta Z_{\mathrm{DR}}}{\Delta Z_{\mathrm{DR}}^{(t)}}\right]^2 + \left[\frac{1-\rho_{\mathrm{hv}}}{\Delta\rho_{\mathrm{hv}}^{(1)}}\right]^2 + \left[\frac{\mathrm{snr}^{(\mathrm{Zdr})}}{\mathrm{snr}}\right]^2 + \left(\frac{\alpha}{50}\right)^2\right\}\right), \tag{15}$$

$$Q_{\rho\mathrm{hv}} = \exp\left(-0.69\left\{\left[\frac{1-\xi}{\Delta\rho_{\mathrm{hv}}^{(2)}}\right]^2 + \left[\frac{1-\rho_{\mathrm{hv}}}{\Delta\rho_{\mathrm{hv}}^{(1)}}\right]^2 + \left[\frac{\mathrm{snr}^{(\rho_{\mathrm{hv}})}}{\mathrm{snr}}\right]^2\right\}\right), \tag{16}$$

$$Q_{\mathrm{KDP}} = \exp\left(-0.69\left\{\left[\frac{\Delta\Phi_{\mathrm{DP}}}{\Delta\Phi_{\mathrm{DP}}^{(t)}}\right]^2 + \left[\frac{1-\rho_{\mathrm{hv}}}{\Delta\rho_{\mathrm{hv}}^{(1)}}\right]^2 + \left[\frac{\mathrm{snr}^{(\mathrm{Kdp})}}{\mathrm{snr}}\right]^2\right\}\right), \tag{17}$$

$$Q_{\mathrm{SDZ}} = \exp\left(-0.69\left\{\left[\frac{\mathrm{snr}^{(\mathrm{SDZ})}}{\mathrm{snr}}\right]^2\right\}\right), \quad \text{and} \tag{18}$$

$$\mathrm{Q}_{\mathrm{SD}\Phi} = \exp\left(-0.69\left\{\left[\frac{\mathrm{snr}^{(\mathrm{Kdp})}}{\mathrm{snr}}\right]^2\right\}\right). \tag{19}$$

In Eqs. (16)–(17), the parameters ξ and $\Delta\Phi_{\mathrm{DP}}$ related to the nonuniform beam filling are specified as in Ryzhkov (2007):

$$\xi = \exp\left\{-1.37\ 10^{-5}\Omega^2\left[\left(\frac{d\Phi_{\mathrm{DP}}}{d\theta}\right)^2 + \left(\frac{d\Phi_{\mathrm{DP}}}{d\varphi}\right)^2\right]\right\} \tag{20}$$

and

$$\Delta\Phi_{\mathrm{DP}} = 0.02\,\Omega^2\left(\frac{d\Phi_{\mathrm{DP}}}{d\theta}\frac{dZ_H}{d\theta} + \frac{d\Phi_{\mathrm{DP}}}{d\varphi}\frac{dZ_H}{d\varphi}\right). \tag{21}$$

In the areas of nonmeteorological echo, high local gradients of Z, Z_{DR}, and Φ_{DP} may produce very large NBF-related biases ΔZ_{DR}, $\Delta\Phi_{\mathrm{DP}}$, and low value of ξ according to Eqs. (10), (21), and (20). In addition, low net values of ρ_{hv} cause significant decreases in the quality factors Q_{ZDR}, $Q_{\rho\mathrm{hv}}$, and Q_{KDP} due to the term

$$\chi = \left[\frac{1-\rho_{\mathrm{hv}}}{\Delta\rho_{\mathrm{hv}}^{(1)}}\right]^2. \tag{22}$$

Observations suggest that ρ_{hv} and Z_{DR} are quite effective in recognizing nonmeteorological echo (hence, the weights for these are relatively high in Table 2) for which intrinsic ρ_{hv} is low; therefore, the decrease of their classification value (due to lowering Q_{ZDR} and $Q_{\rho\mathrm{hv}}$) is counterproductive. To mitigate the negative influence of these factors on the classification quality of nonmeteorological echo, it is recommended to enhance Q_{ZDR} and $\mathrm{Q}_{\rho\mathrm{hv}}$ using the following settings:

$$\Delta Z_{\mathrm{DR}} = 0, \quad \xi = 1, \quad \chi = 0 \quad \textit{if}\ \rho_{\mathrm{hv}} < 0.8. \tag{23}$$

The biases of Z and Z_{DR} due to radar miscalibration can be estimated from data analysis using consistency between Z, Z_{DR}, and K_{DP} in rain and utilizing measurements in light rain or dry aggregated snow, which may serve as natural calibrators for Z_{DR} (e.g., Ryzhkov et al. 2005a). However, such an assessment is not always possible. For example, the use of K_{DP} for the consistency check requires rain of relatively high intensity. For this reason radar miscalibration errors are not currently involved in the estimation of the factors Q_Z and $\mathrm{Q}_{\mathrm{ZDR}}$, although all possible measures are undertaken to minimize system biases in Z and Z_{DR}.

4. Class designation

Because the membership functions of some classes of liquid and frozen hydrometeors (such as rain and dry snow) heavily overlap, the classification of these elements can be significantly improved by taking into account the location of the radar resolution volume with respect to the melting layer. The top and bottom of the melting layer can be determined from an upper-air sounding, numerical model output, or from polarimetric data (if echoes cover a sufficiently large area). The melting layer detection algorithm (MLDA) developed at NSSL determines the top and bottom of the melting

layer as a function of the azimuth for any given radar scan (Giangrande et al. 2008). The MLDA identifies radar ranges where ρ_{hv} is between 0.90 and 0.97 for elevation angles between 4° and 10°. If the maxima of Z between 30 and 47 dBZ and Z_{DR} between 0.8 dB and 2.5 dB are observed in a 500-m-thick horizontal layer just above the height of the range gate where $0.90 < \rho_{hv} < 0.97$, then this range and its corresponding height identify the melting layer. This routine is repeated for each azimuth and the resulting cluster of melting layer points is used to determine the top (H_t) and bottom (H_b) heights of the melting layer as functions of the azimuth.

Checking the consistency of the designated class with the location of the melting layer is an important part of the classification routine. The geometry of the radar beam with respect to the melting layer is illustrated in Fig. 2; the slant ranges R_b and R_t correspond to geometrical projections of the melting layer onto the cone generated by the beam center at the lowest tilt. In fact, mixed-phase hydrometeors partially fill the radar resolution volume in a much broader interval of ranges (R_{bb}, R_{tt}) due to the antenna beamwidth. Once the boundaries of the melting layer are determined, the fuzzy logic aggregation (3) and classification procedure are applied with two restrictions: snow is not allowed below the ML bottom and pure rain is prohibited above the ML top except for the big-drops category; these are commonly transported by convective updrafts well above the environmental freezing level.

The following subsets of classes are allowed within five slant range intervals:

$$
\begin{aligned}
&0 < R < R_{bb}\text{—GC/AP, BS, BD, RA, HR, RH;}\\
&R_{bb} < R < R_{b}\text{—GC/AP, BS, WS, GR, BD, RA, HR, RH;}\\
&R_{b} < R < R_{t}\text{—GC/AP, BS, DS, WS, GR, BD, RH;}\\
&R_{t} < R < R_{tt}\text{—GC/AP, BS, DS, WS, CR, GR, BD, RH; and}\\
&R > R_{tt}\text{—DS, CR, GR, RH.}
\end{aligned}
\tag{24}
$$

Additional routines in the HCA include separation of convective and stratiform echoes, checks if the results are reasonable, and despeckling. Identifying convective and stratiform parts of a radar echo helps to better discriminate between wet snow and melting graupel within the melting layer. The algorithm for identifying convective echoes is similar to the method developed by Zhang et al. (2008). It is based on detecting high values

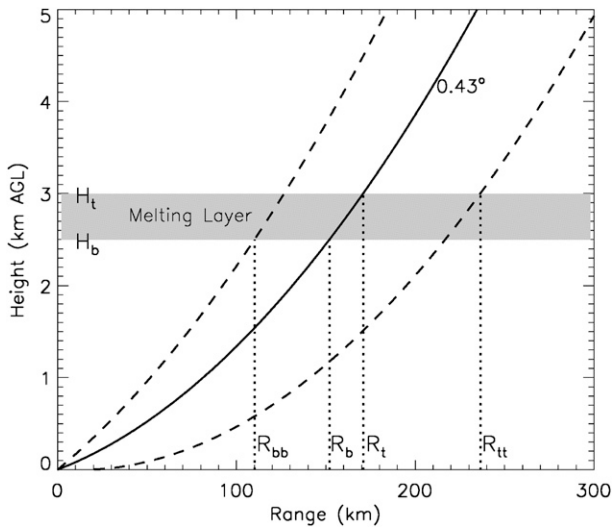

FIG. 2. Geometry of the radar beam with respect to the melting layer. The beam axis is drawn with the thick solid line whereas the locations of the ±0.5° beam extent (3-dB beamwidth) are indicated with the dashed curves. Dotted lines indicate slant ranges R_{bb}, R_b, R_t, and R_{tt}, corresponding to geometrical projections of the melting layer from the radar beam onto the base tilt. The heights H_b and H_t represent the melting layer bottom and top heights, respectively.

in the observed vertical profiles of reflectivity and the top of the melting layer (typically coincident with the 0°C wet-bulb temperature height) derived from polarimetric variables. Polarimetric data with ρ_{hv} less than 0.85 are considered to be contaminated by nonmeteorological scatterers (Giangrande and Ryzhkov 2008) and are tagged prior to the convective identification procedure. To discriminate between convective and stratiform echoes, the radar reflectivity at a given slant range and azimuth is examined for all elevations. This slant range and azimuth are identified as belonging to the convective echo if the maximum reflectivity in the vertical column is higher than 45 dBZ or Z is higher than 30 dBZ at altitudes of 1.6 km or higher above the melting layer top. If the echo is classified as convective, then dry snow and wet snow (DS and WS) are not allowed within a whole vertical column. Conversely, the "convective" hydrometeor types such as BD, GR, and RH are excluded in the stratiform case.

To check if the results are reasonable, a set of "hard thresholds" is used, thereby reducing the number of clearly wrong class designations; for example, hail is considered to be misclassified if $Z < 40$ dBZ. In such cases the algorithm accepts the class with the next highest aggregation value. The set of such checks or rules is presented in Table 3. These checks are based on physical models and the results of observations and are

TABLE 3. Empirical hard thresholds used to suppress apparently wrong designations. Function $f_2(Z)$ is determined by Eq. (4).

Variables	Thresholds	Suppressed class
V	>1 m s^{-1}	GC/AP
ρ_{hv}	>0.97	BS
Z_{DR}	>2 dB	DS
Z	<20 dBZ	WS
Z_{DR}	<0 dB	WS
Z	>40 dBZ	CR
Z	<10 Z or >60 dBZ	GR
Z_{DR}	$<f_2(Z) - 0.3$	BD
Z	>50 dBZ	RA
Z	<30 dBZ	HR
Z	<40 dBZ	RH

consistent with the results in the Straka et al. (2000) overview.

The despeckling procedure eliminates isolated incidents of misclassification within fields of relatively uniform classes, hence producing a less noisy outcome.

5. Results of classification for the MCS case on 13 May 2005

The performance of the HCA is illustrated for the case of an MCS that developed over northwestern Oklahoma and moved eastward through central Oklahoma on 13 May 2005. The storm was observed by the National Oceanic and Atmospheric Administration (NOAA)/NSSL polarimetric ''proof of concept'' WSR-88D radar (KOUN hereafter). KOUN data were collected at 15 antenna elevations (0.0°, 0.43°, 1.4°, 2.5°, 3.5°, 4.5°, 5.5°, 6.5°, 7.5°, 8.7°, 10.0°, 12.0°, 14.0°, 16.7°, and 19.5°) with a volume update time of about 6 min. Absolute calibration of Z was made by checking its consistency with K_{DP} measurements (Ryzhkov et al. 2005a) in areas of moderate to heavy rain with $Z > 40$ dBZ and via cross comparison with the operational Oklahoma City, Oklahoma (KTLX), WSR-88D radar, which is located about 20 km from KOUN. Following Ryzhkov et al. (2005a), the differential reflectivity was calibrated using the measurements of Z_{DR} in dry aggregated snow slightly above the melting layer in the stratiform part of the MCS. Future calibration on the operational dual-polarization radar network will be automated (at the end of each volume scan as is done presently for reflectivity measurements). This will be augmented by more extensive checks daily and monthly. Similar approaches will be used for the differential reflectivity whereby the augmented checks will involve comparisons with sun scans. These approaches were not available at KOUN in May 2005. Hence, the manual and postoperational calibrations were required.

a. Estimation of the confidence vector

Gradients of Z and Z_{DR}, and values of ρ_{hv}, SNR, and Φ_{DP} all affect the confidence vector. Figure 3 shows a composite 0.43° elevation plan position indicator (PPI) display of Z, Z_{DR}, Φ_{DP}, ρ_{hv}, and SNR at 0646 UTC. A decrease in ρ_{hv} along the southern flank of the squall line is notable at distances beyond 140–150 km. This is a clear manifestation of nonuniform beam-filling effects, which were estimated from the analysis of the vertical and horizontal gradients of Z, Z_{DR}, and ρ_{hv} as prescribed by Eqs. (10), (20), and (21). The gradients were computed from the differences between the radar variables at adjacent radials spaced by 1° in the azimuth and the elevation. Antenna elevations of 0.43° and 1.4° were used to compute the vertical gradients. Large vertical and azimuthal gradients of the differential phase at longer distances along the squall line contribute significantly to the biases in ρ_{hv} and Φ_{DP} (Fig. 4), with the vertical gradient of Φ_{DP} being primarily responsible for the large NBF-related errors in this area. The NBF bias in Z_{DR} is highest within the melting layer (Fig. 4) because vertical gradients of Z and Z_{DR} are high there [see Eq. (10)].

The fields of the confidence factors of Z, Z_{DR}, K_{DP}, and ρ_{hv} are displayed in Fig. 5. The confidence factors Q_Z, Q_{ZDR}, Q_{KDP}, and $Q_{\rho hv}$ were determined using Eqs. (14)–(17), where

$$\begin{aligned} &\Phi_{DP}^{(Z)} = \Phi_{DP}^{(Zdr)} = 250°, \quad \Delta\Phi_{DP}^{(t)} = 10°, \\ &\Delta\rho_{hv}^{(1)} = 0.2, \quad \Delta\rho_{hv}^{(2)} = 0.1, \quad \Delta Z_{DR}^{(t)} = 0.5 \text{ dB}, \\ &\text{SNR}^{(Z)} = \text{SNR}^{(Kdp)} = 0 \text{ dB}, \quad \text{and} \\ &\text{SNR}^{(Zdr)} = \text{SNR}^{(\rho hv)} = 5 \text{ dB}. \end{aligned} \tag{25}$$

The choice of threshold parameters in (25) was based on a theoretical analysis of the measurement errors caused by low ρ_{hv} and SNR (Bringi and Chandrasekar 2001; Melnikov and Zrnić 2007) and NBF (Ryzhkov 2007).

As can be deduced from Eqs. (14)–(17), the confidence factors of the three polarimetric variables are mainly affected by NBF and the magnitude of ρ_{hv}, which determines the noisiness of the polarimetric measurements. For this reason, the largest drop in the confidence factors for Z_{DR}, K_{DP}, and ρ_{hv} is observed in the areas of the large gradients of Φ_{DP} (west-southwest from the radar) and within the melting layer where intrinsic values of the cross-correlation coefficients are low. All confidence factors decrease at the periphery of the radar echo due to a reduction in the signal-to-noise ratio. The radar reflectivity is less affected by this reduction compared to polarimetric variables and therefore is the most reliable classification parameter in the areas of weak weather radar echo.

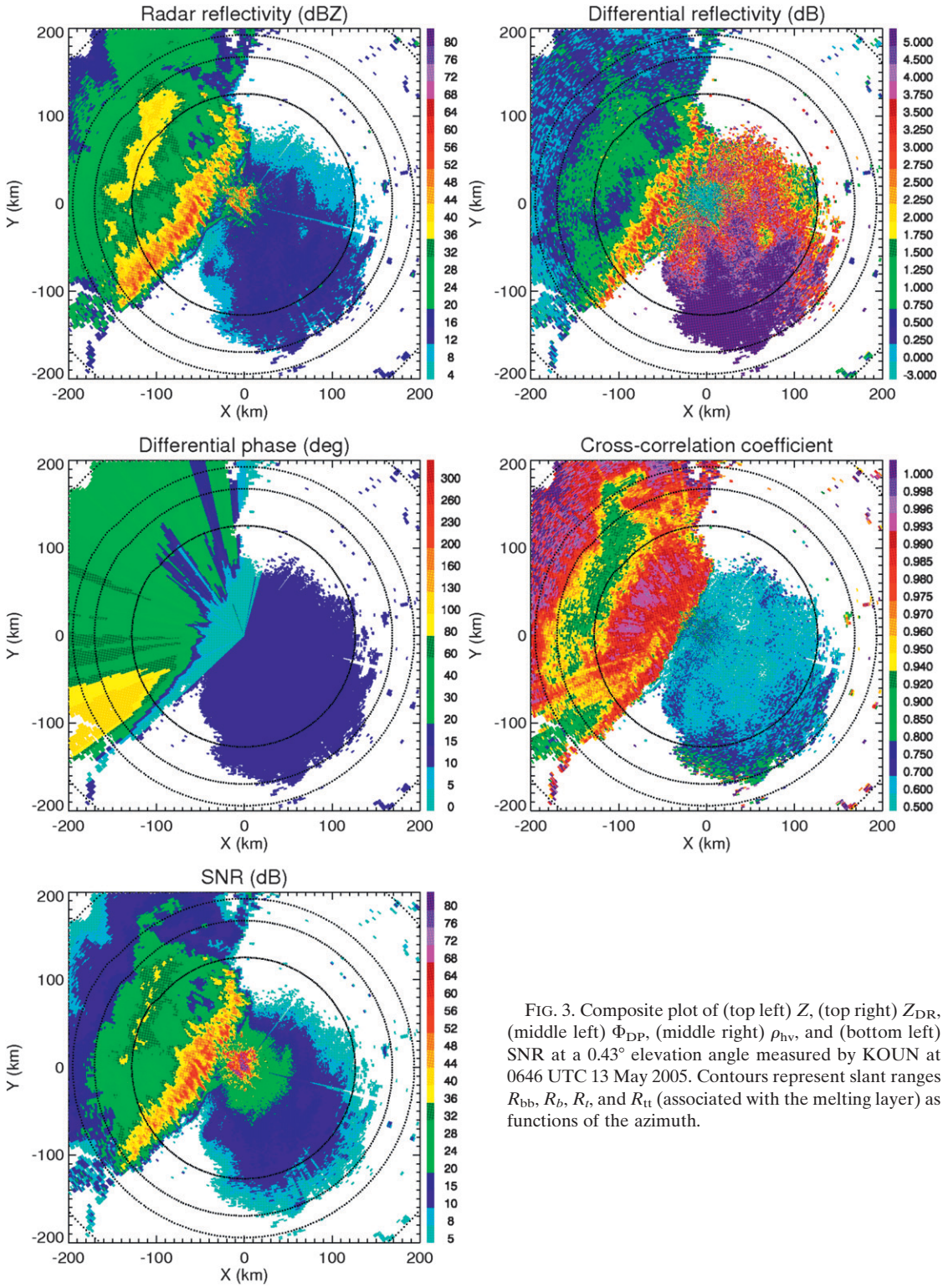

FIG. 3. Composite plot of (top left) Z, (top right) Z_{DR}, (middle left) Φ_{DP}, (middle right) ρ_{hv}, and (bottom left) SNR at a 0.43° elevation angle measured by KOUN at 0646 UTC 13 May 2005. Contours represent slant ranges R_{bb}, R_b, R_t, and R_{tt} (associated with the melting layer) as functions of the azimuth.

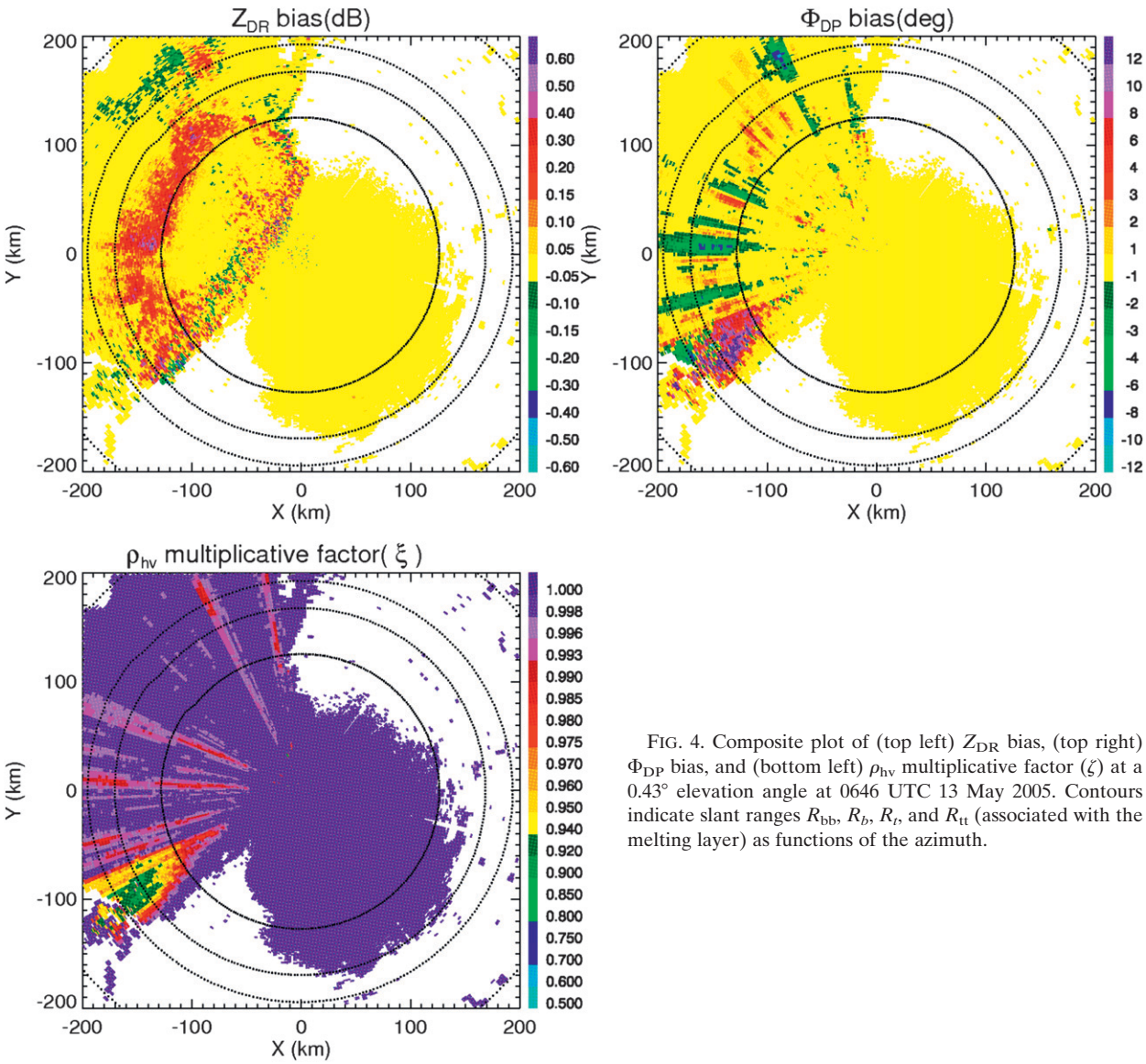

FIG. 4. Composite plot of (top left) Z_{DR} bias, (top right) Φ_{DP} bias, and (bottom left) ρ_{hv} multiplicative factor (ζ) at a 0.43° elevation angle at 0646 UTC 13 May 2005. Contours indicate slant ranges R_{bb}, R_b, R_t, and R_{tt} (associated with the melting layer) as functions of the azimuth.

In the region of clear-air echo (SE quadrant), the confidence factors for Z and K_{DP} are almost identical because both are primarily determined by SNR as condition (23) is applied. The confidence factors for Z_{DR} and ρ_{hv} are alike in that region for the same reason.

b. *Melting-layer detection*

Once the confidence factors are determined and aggregation values are computed, the top and bottom of the melting layer are estimated at each azimuth to constrain the classes into the permissible subsets listed in (24).

Figure 6 displays the melting-layer polarimetric signatures at an elevation of 4.5° at 1016 UTC. Note that both the Z_{DR} and ρ_{hv} signatures of the melting layer are well depicted in the convective part of the storm in the SE sector where a conventional radar reflectivity factor shows only a hint of the bright band. The outcome of the routine for estimating the melting-layer top and bottom heights H_t and H_b suggested by Giangrande et al. (2008) is illustrated in Fig. 7a. In each azimuthal direction, a histogram of the heights of the radar resolution volumes belonging to the melting layer (i.e., ML points displayed as black dots in Fig. 7a) is examined and its 20% and 80% percentiles are utilized to define H_t and H_b. The corresponding contours of R_{bb}, R_b, R_t, and R_{tt} determined in Fig. 2 are overlaid in Figs. 3–5.

According to Giangrande et al. (2008), the top of the melting layer derived from polarimetric measurements approximates the height of the 0° wet-bulb temperature with an RMS error of about 0.2 km in most cases.

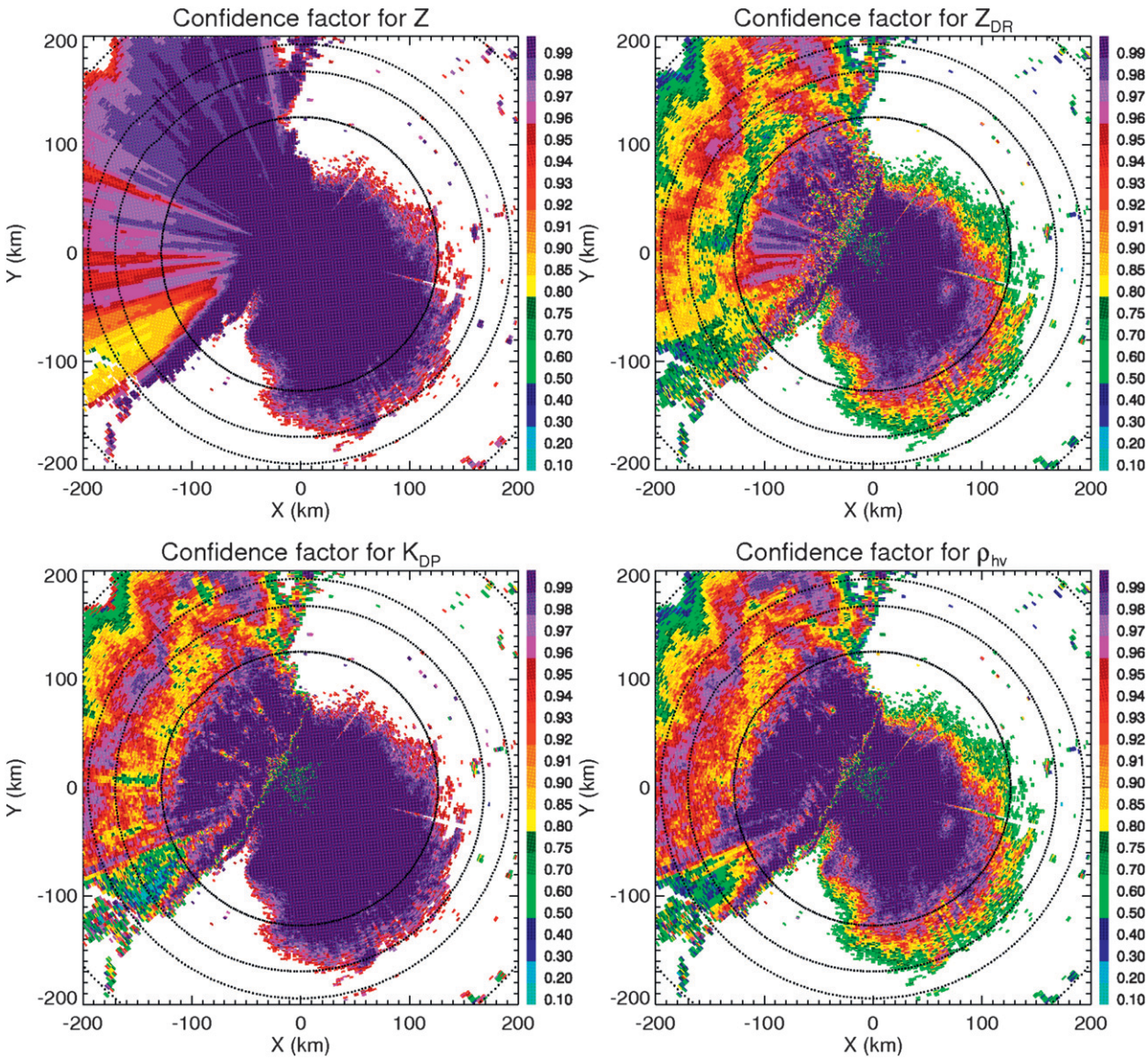

FIG. 5. Composite plot of the confidence factors of (top left) Z, (top right) Z_{DR}, (bottom left) K_{DP}, and (bottom right) ρ_{hv} at a 0.43° elevation angle at 0646 UTC 13 May 2005. The slant ranges R_{bb}, R_b, R_t, and R_{tt} (associated with the melting layer) as functions of azimuth are overlaid on the image as contours.

Comparison with sounding data obtained near the radar location at 1200 UTC in clear atmosphere after the storm passed over the radar (Fig. 7b) indicates that the mean ML top (averaged over all azimuths) is at the temperature of about 2°C, or 300 m below the 0°C isotherm. Such a discrepancy is attributed to relatively low humidity (70%–80%) at the 0°C isotherm level; hence, the wet-bulb temperature is still below zero at this height. In fact, the difference between the measured temperature and the wet-bulb temperature is about 2°C. Melting starts where wet-bulb temperature exceeds 0°C (dash–dot line in Fig. 7b).

c. *Classification results*

HCA output at the base elevation of 0.43° is displayed in Fig. 8 for 0646 and 0934 UTC. Although it is not possible to verify the HCA output by comparisons with in situ measurements, the results of the classification in both panels in Fig. 8 fit the accepted microphysical conceptual models of trailing stratiform MCSs (Houze et al. 1989). At 0646 UTC, biological scatterers and ground clutter (two shades of blue) are identified ahead of the squall line. The leading edge of the squall line is marked by a thin line of big drops associated with size

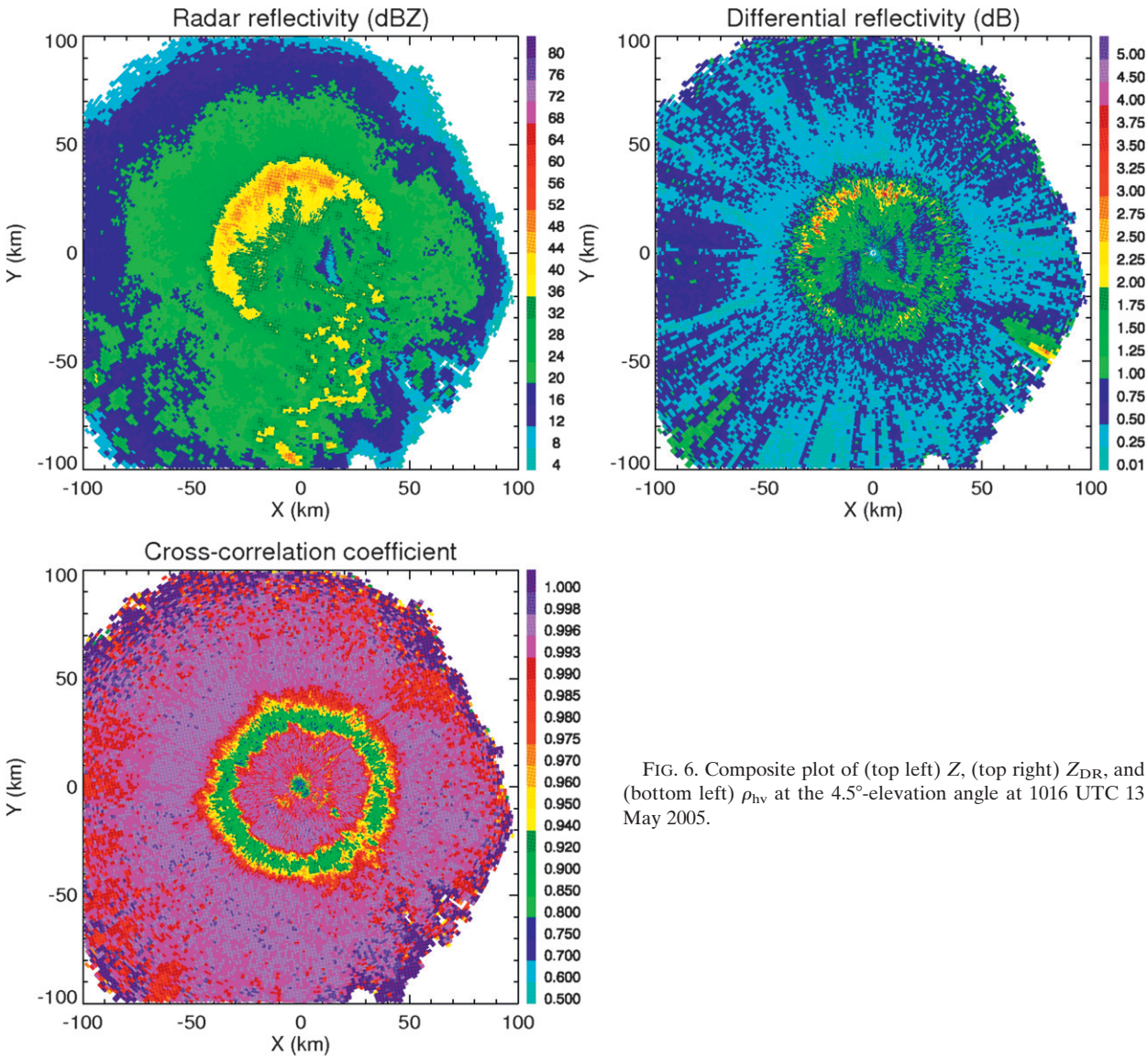

FIG. 6. Composite plot of (top left) Z, (top right) Z_{DR}, and (bottom left) ρ_{hv} at the 4.5°-elevation angle at 1016 UTC 13 May 2005.

sorting caused by updrafts and wind shear (Wakimoto and Bringi 1988; Kumjian and Ryzhkov 2008). It is followed by heavy rain (dark shade of red) and occasional regions of hail (pink). A gradual transition from rain to wet snow (green), dry snow (blue), and crystals (dark shade of green) is clear in the stratiform part of MCS once the radar beam approaches and overshoots the melting level. Elevated areas of graupel (yellow) are evident in the convective part of the storm at its southern flank.

Three hours later, at 0934 UTC, convective updrafts persist along the leading edge of the squall line. Ahead of the convective core of precipitation is the edge of the gust front, which, according to the algorithm, contains biological scatterers. Graupel at heights over 2 km above ground and hail are also identified at the southern flank of the storm, whereas the transition from rain to wet snow, dry snow, and crystals is preserved at its northern flank. Notable is the appearance of the ground clutter behind the storm, which is caused by superrefraction (anomalous propagation) in the post-MCS environment.

To evaluate the impacts of newly added features on the performance of HCA, we compare the classification results obtained with the latest version of the classification algorithm in Fig. 8 with the outputs of two aborted versions of HCA (Fig. 9). In both simplified versions, all elements of the matrix of weights **W** and the confidence vector **Q** are set to 1, antenna beam broadening is not taken into account, and no vertical continuity check is performed to distinguish between the convective and stratiform parts of the storm. The top

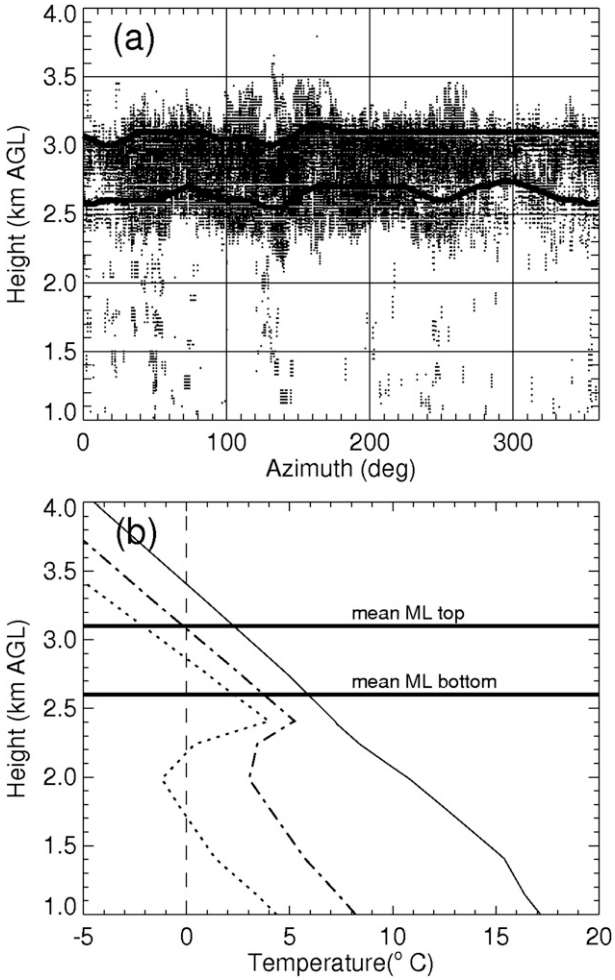

FIG. 7. Results of (a) the polarimetric melting-layer detection for the volume scan illustrated in Fig. 6 and (b) the sounding. In (a), ML top and bottom heights AGL are displayed with thick solid lines. In (b), the temperature (thin solid line), dewpoint (dotted line), and wet-bulb temperature (dashed–dotted line) are plotted from sounding data launched near KOUN at 1200 UTC 13 May 2005; the mean ML top and bottom heights designated from the radar are superimposed with thick solid lines and the 0°C line is plotted with a vertical dashed line.

panels in Fig. 9 illustrate the results of the classification if no information about the melting layer is taken into consideration. This information was utilized to make the HCA outputs shown in the bottom panels of Fig. 9. Note that the membership functions $P^{(i)}(V_j)$ were the same for all three versions of HCA.

There are similarities and significant differences between the classification products in Figs. 8 and 9. All three versions of HCA reliably distinguish between meteorological and nonmeteorological radar echoes and identify heavy rain and hail in the same areas. However, the designations of other hydrometeor classes are vastly different. Numerous false designations of frozen particles (such as dry snow or crystals) below the freezing level are visible in the HCA product if the information about melting layer is ignored (top panels in Fig. 9). This is due to the fact that the membership functions corresponding to some categories of liquid and frozen hydrometeors heavily overlap (see Table 1). Incorporating information about the melting layer helps to mitigate this deficiency, but ignoring antenna beam broadening results in artificial circular boundaries and in underestimating the impact of the wet snow contribution on the radar polarimetric variables. The areas of rain and snow in Fig. 8 look more uniform and contain fewer speckles compared to the corresponding areas in Fig. 9 due to the application of weights, confidence factors, vertical continuity checks, and the hard thresholds from Table 3. Overall, the comparison of Figs. 8 and 9 shows that supplementary routines and checks added to the "core fuzzy logic procedure" with the same membership functions have a significant impact on the results of the classification.

Although the classification results presented in Fig. 8 seem quite reasonable, some deficiencies are also noticeable. These include apparent misclassifications at the two NE azimuthal directions (right panel in Fig. 8) where partial beam blockage occurs due to two towers, the impact of which cannot be accounted for using the digital elevation map, that is, utilizing factor α in Eqs. (14) and (15). Another concern is the appearance of rain within the melting layer and the artificial-looking boundary along R_b at the northern flank of the MCS in the left panel in Fig. 8. These and other potential shortcomings will be addressed in future enhancements to the HCA.

Classification is performed at each antenna elevation and two vertical cross sections of the results constructed from the series of conical scans are in Figs. 10 and 11 . In Fig. 10, the bright band is identified as wet snow (light green) and separates dry snow and rain in the stratiform part of the storm. In the storm's convective part, graupel is shown in yellow and hail in pink. Hail is aloft (two small areas) and likely melts completely before reaching the ground. Ice crystals abound at more than 2 km above ground while dry snow is prevalent at over 3.1 km; biological scatterers are recognized in the boundary layer ahead of the storm at distances beyond 95 km from the radar.

In the more intense part of the storm illustrated in Fig. 11, the bulk of the hydrometeors identified as graupel and large drops fill a larger volume than in the less intense part (Fig. 10). A vertical Z_{DR} column, which is clearly visible between 40 and 50 km and collocated with a region of relatively low reflectivity, is associated with big drops that are suspended in a convective updraft. Again, two vertically elongated regions in the

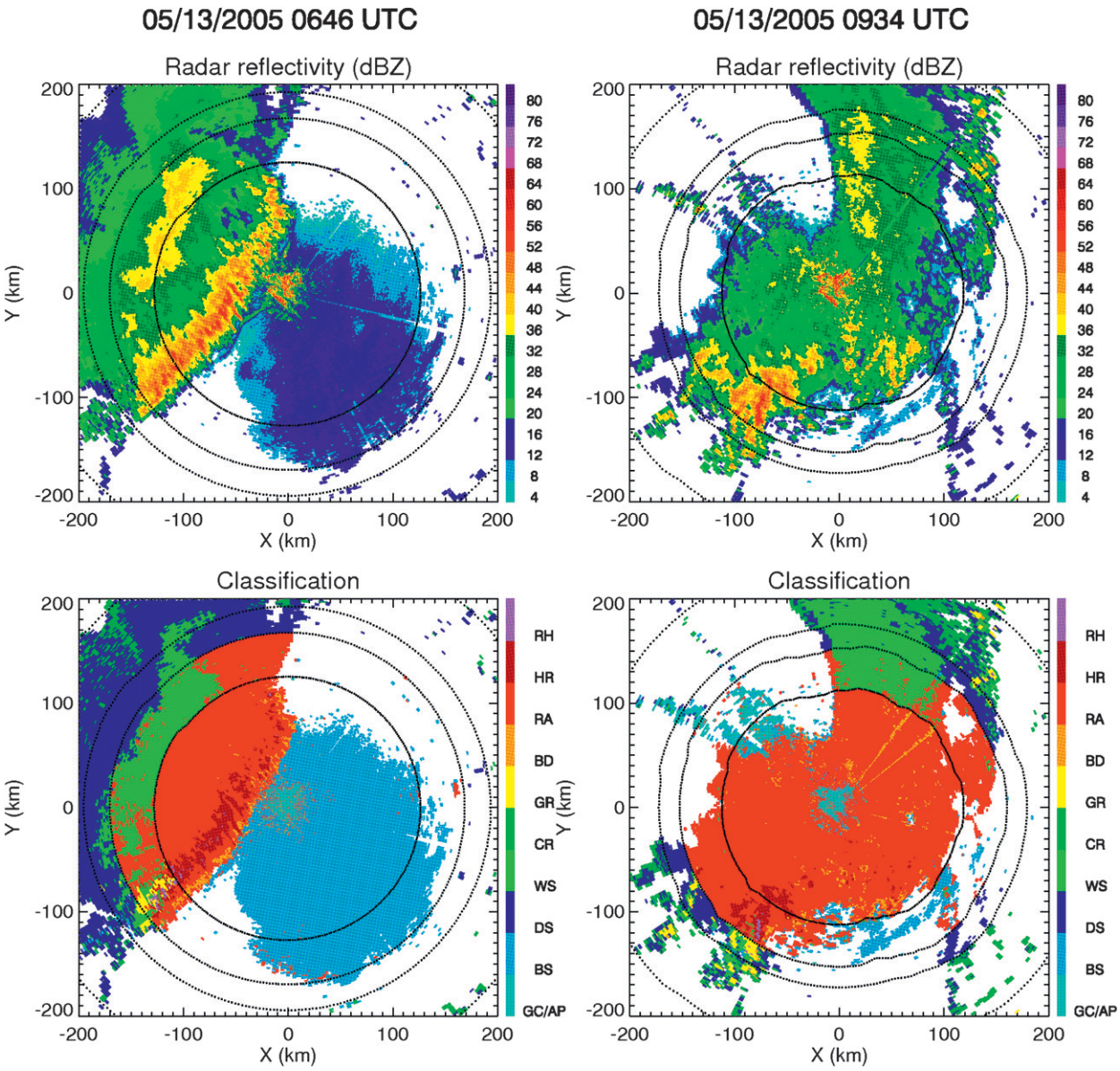

FIG. 8. Fields of (top) radar reflectivity and (bottom) classification results displayed as a PPI at the 0.43° elevation angle at (left) 0646 and (right) 0934 UTC on 13 May 2005. Contours indicate slant ranges R_{bb}, R_b, R_t, and R_{tt} (associated with the melting layer) as functions of the azimuth.

height interval between 1 and 3.5 km are recognized as a hail–rain mixture (pink).

These examples illustrate how HCA provides new, important information for operational meteorologists. First of all, it clearly delineates meteorological and nonmeteorological echoes including the one caused by the anomalous propagation in the areas of cold thunderstorm outflow (right panel in Fig. 8). It allows for monitoring of the height and depth of the melting layer and their changes due to frontal passages. Indeed, the comparison of the dotted circular curves in the left and right panels of Fig. 8 indicates that the melting layer descends in the course of 3 h; that is, the radii of the curves become smaller. This corresponds to the decrease of the melting-layer height by more than 0.6 km. Detection of the melting layer, which often descends to the ground during the cold season, is crucial for delineating rain and snow in winter storms (Ryzhkov and Zrnić 1998).

The big-drop signature is especially helpful for assessing the stage of convective development. Indeed, "Z_{DR} columns," which may be identified with the HCA as big drops above the freezing level, signify updrafts

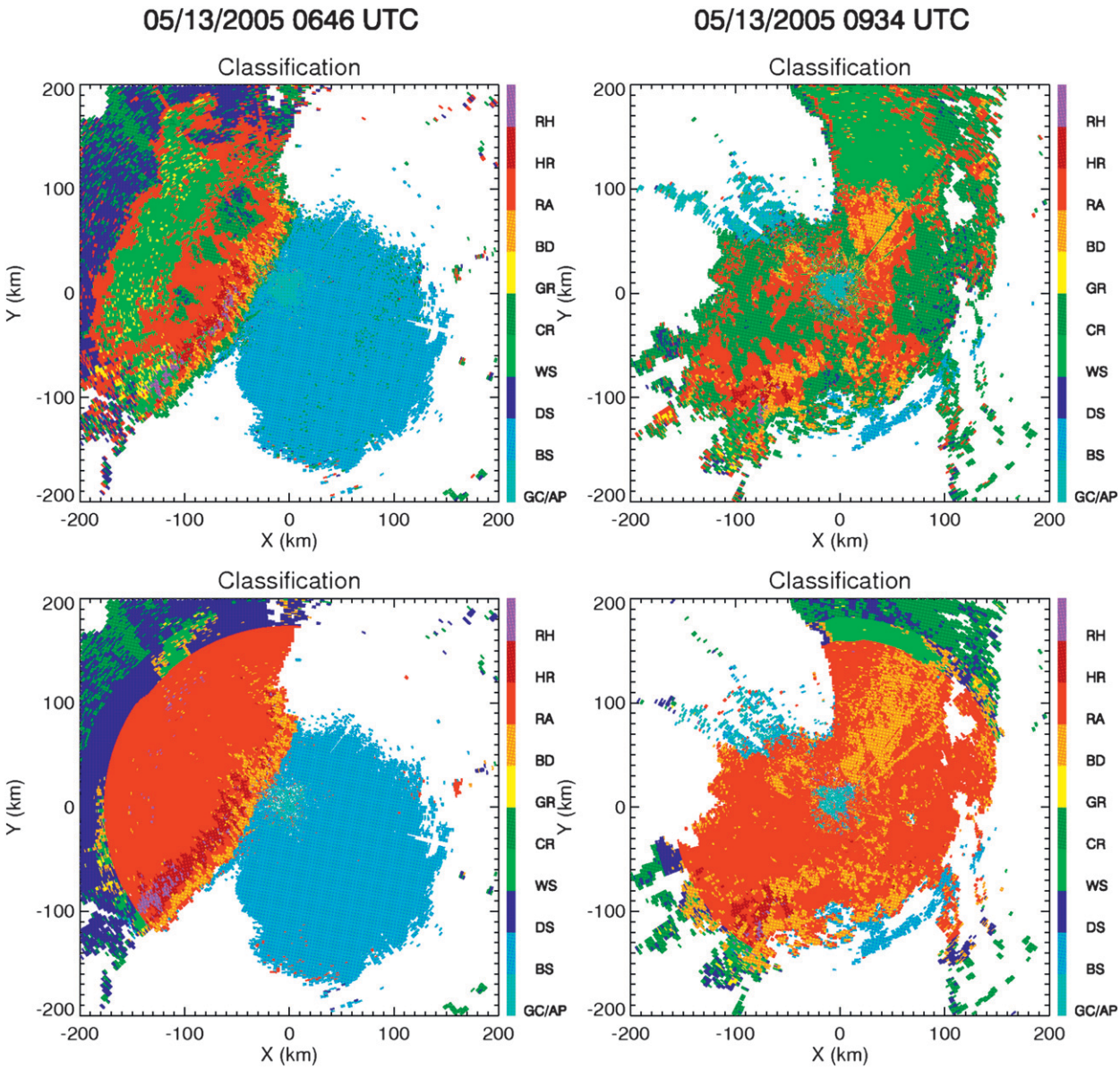

FIG. 9. As in Fig. 8, but here the classification was performed with two aborted versions of HCA: (all panels) beam broadening is not taken into account, and there is no vertical continuity check **W**= 1, **Q**= 1; (top) melting layer information is not used; and (bottom) melting layer information is utilized.

and convective initiation. The areas of big drops at the leading edge of the squall line (left panel in Fig. 8) manifest three microphysical processes: differential sedimentation at the onset of precipitation (larger raindrops fall faster and reach the surface ahead of smaller ones), unidirectional wind shear, and size sorting within an updraft. In the case of a supercell storm, the big-drop signature in the southern part of the forward-flank downdraft signifies veering of the wind and enhanced storm-relative helicity (Kumjian and Ryzhkov 2008). It should be noted that melting graupel–hail in the storm downdrafts also may produce very high Z_{DR}, which is usually associated with high Z and is not classified by our scheme as big drops.

The graupel and rain–hail categories help to pinpoint locations of possible hail development and help to monitor how hail descends to the ground, as seen in Figs. 10 and 11. In addition to monitoring descending hail, HCA can also help determine if hail melts prior to reaching the ground by examining the lowest HCA tilt. If there is no hail on the lowest tilt below the melting layer, then no hail should be reaching the ground.

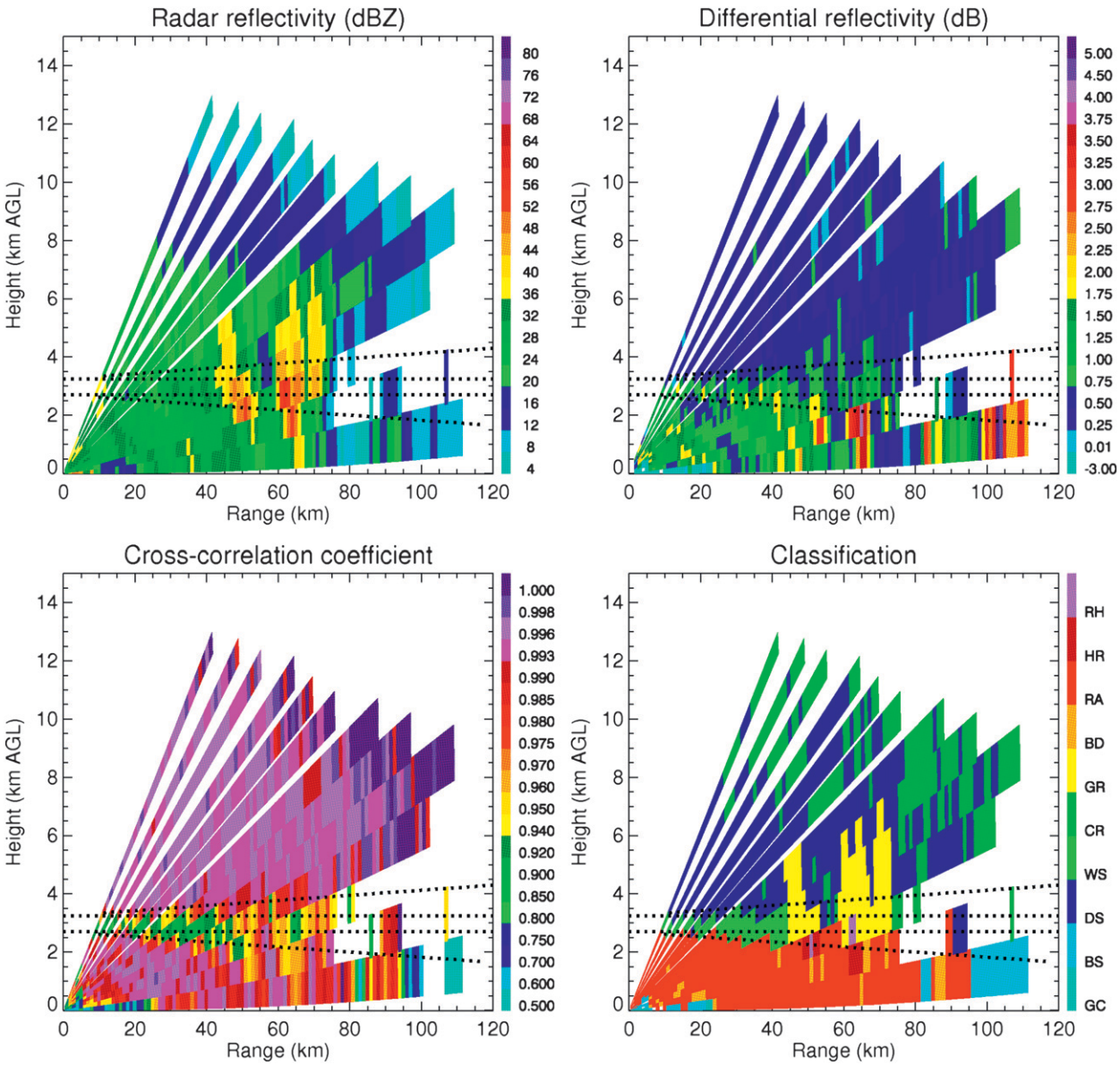

FIG. 10. Composite plot of (top left) Z, (top right) Z_{DR}, (bottom left) ρ_{hv}, and (bottom right) the results of hydrometeor classification in the RHI cross section at 1013 UTC 13 May 2005. The azimuth angle is 156°. Dotted lines indicate slant ranges R_{bb}, R_b, R_t, and R_{tt} (associated with the melting layer) at the azimuth.

In addition to the information provided for operational forecasters, the classification product greatly benefits quantitative precipitation estimation because it reveals the appropriate rainfall relation that should be applied to the observed hydrometeor class (Giangrande and Ryzhkov 2008).

6. Summary and conclusions

A proposed methodology for classifying hydrometeors using dual-polarization WSR-88D radars is presented. The algorithm builds on several previous versions and has been accepted for the first software release on the upgraded network. It enables discrimination between 10 different classes (rain, heavy rain, rain/hail, big drop, wet snow, dry snow, graupel, crystals, biological scatterers, and ground clutter); hence, it can be used to discriminate between hydrometeor types in both warm-season and cold-season precipitation systems. The main goal of the improved version is to provide users with a product that identifies important precipitation classes (hail, heavy rain, attributes of the

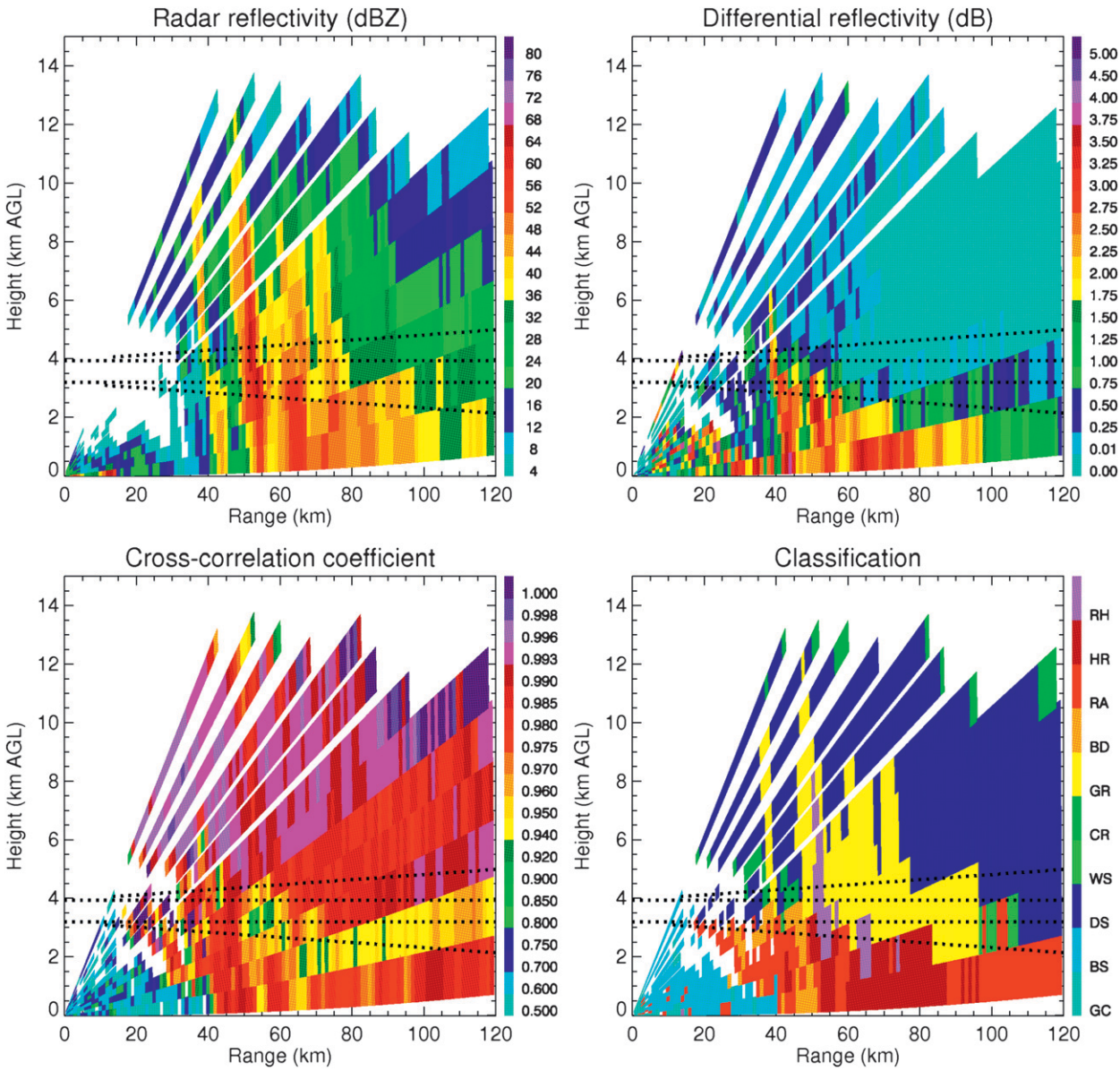

FIG. 11. As in Fig. 10, except the data are taken at 0646 UTC 13 May 2005 and the azimuth angle is 252°.

melting layer) while minimizing the occurrence of obvious misclassifications. Novel features have been introduced to meet this goal.

The first new feature introduced is the confidence vector, which quantifies the quality of each radar variable estimate. Nonuniform beam filling, attenuation, statistical errors, partial beam blockage, and noise all affect the quality of the classification scheme. The impacts of all of these factors on radar measurements are gauged using Gaussian functions as additional weights in the fuzzy logic scheme. It is possible to use the confidence factor statistically by assigning a threshold that, if exceeded, indicates that the classification results are acceptable; this nonetheless has not been done in the present study.

Next, the algorithm applies a matrix of weights so that each pair of a radar variable (six) and class (ten) gets a unique weight. The weights are chosen to favor a class that the value of the variable can identify particularly well. In this manner the classification potency of a variable to characterize a particular hydrometeor class is exploited.

The algorithm also determines the top and bottom heights of the melting layer for every azimuthal angle about the radar site. It then combines the principles of

class designation relative to the location of the melting layer with the fuzzy logic approach, taking into account the broadening of the radar beam at longer distances. This can make the separation of liquid and frozen hydrometeors much more realistic. As a consequence, it is possible to provide a higher probability of correct classification and reduce the occurrence of apparently erroneous class designations in the field of classification results.

Finally, vertical continuity checks are applied to better distinguish between convective parts of the storm associated with dry–wet graupel aloft and its stratiform region where rain originates from dry–wet snow at higher levels. This improves the level of discrimination between graupel and snow.

The hydrometeor classification algorithm was applied to the mesoscale convective system observed with the KOUN radar on 13 May 2005. The results of the classification effectively show heavy rain (occasionally mixed with hail) and graupel in the convective part of the MCS, big drops along the leading edge of the squall line, and a gradual transition from rain to wet snow, dry snow, and crystals in its trailing stratiform region as the height of the radar sampling volume increases with distance. Ground clutter (including that due to anomalous propagation) and biological scatterers ahead of the storm are also reliably recognized.

Classification output obtained from polarimetric radar can be very helpful in the forecast process. It provides operational meteorologists information about the origin of a radar echo, the height and depth of the melting layer, the stage of convective development, the localization of vertical flows (updrafts–downdrafts), strong wind shear, and rotation, as well as the capability for monitoring the development and location of hail.

Although the suggested algorithm demonstrates agreement with conceptual models of MCSs and provides reasonable classification results for the MCS case on 13 May 2005 (and similar warm-season cases not described in the paper), there is room for improvement. Application to a wider range of weather events, including cold-season storms with low melting layers or the lack of a melting layer, will be examined in future studies.

Acknowledgments. We express out thanks to Scott Giangrande and Matthew Kumjian for helpful suggestions. Terry Schuur, Kimberly Elmore, and an anonymous reviewer provided comments that have strengthened this manuscript. Paul Schlatter's extensive and useful review is appreciated as it helped in improving the paper. This work was funded by the NOAA/Office of Oceanic and Atmospheric Research under NOAA–University of Oklahoma Cooperative Agreement NA17RJ1227, the U.S. Department of Commerce, and by the U.S. National Weather Service, Federal Aviation Administration, and Department of Defense program for modernization of NEXRAD radars. The lead author was partially supported by the Korea Meteorological Administration Research and Development Program under Grant CATER 2007-2104. The authors thank the NSSL/CIMMS employees who maintain and operate the KOUN polarimetric radar for research-grade applications.

REFERENCES

Bringi, V. N., and V. Chandrasekar, 2001: *Polarimetric Doppler Weather Radar: Principles and Applications*. Cambridge University Press, 636 pp.

Giangrande, S. E., and A. V. Ryzhkov, 2005: Calibration of dual-polarization radar in the presence of partial beam blockage. *J. Atmos. Oceanic Technol.,* **22,** 1156–1166.

——, and ——, 2008: Estimation of rainfall based on the results of polarimetric echo classification. *J. Appl. Meteor. Climatol.,* **47,** 2445–2462.

——, J. M. Krause, and A. V. Ryzhkov, 2008: Automatic designation of the melting layer with a polarimetric prototype of the WSR-88D radar. *J. Appl. Meteor. Climatol.,* **47,** 1354–1364.

Heinselman, P. L., and A. V. Ryzhkov, 2006: Validation of polarimetric hail detection. *Wea. Forecasting,* **21,** 839–850.

Houze, R. A., Jr., S. A. Rutledge, M. I. Biggerstaff, and B. F. Smull, 1989: Interpretation of Doppler weather radar displays of midlatitude mesoscale convective systems. *Bull. Amer. Meteor. Soc.,* **70,** 608–619.

Keenan, T. D., 2003: Hydrometeor classification with a C-band polarimetric radar. *Aust. Meteor. Mag.,* **52,** 23–31.

Kumjian, M. R., and A. V. Ryzhkov, 2008: Polarimetric signatures in supercell thunderstorms. *J. Appl. Meteor. Climatol.,* **47,** 1940–1961.

Lim, S., V. Chandrasekar, and V. N. Bringi, 2005: Hydrometeor classification system using dual-polarization radar measurements: Model improvements and in situ verification. *IEEE Trans. Geosci. Remote Sens.,* **43,** 792–801.

Liu, H., and V. Chandrasekar, 2000: Classification of hydrometeors based on polarimetric radar measurements: Development of fuzzy logic and neuro-fuzzy systems, and in situ verification. *J. Atmos. Oceanic Technol.,* **17,** 140–164.

Marzano, F., D. Scaranari, M. Montopoli, and G. Vulpiani, 2008: Supervised classification and estimation of hydrometeors from C-band dual-polarized radars: A Bayesian approach. *IEEE Trans. Geosci. Remote Sens.,* **46,** 85–98.

Melnikov, V. M., and D. S. Zrnić, 2007: Autocorrelation and cross-correlation estimators of polarimetric variables. *J. Atmos. Oceanic Technol.,* **24,** 1337–1350.

Park, H.-S., A. V. Ryzhkov, D. S. Zrnić, and K.-E. Kim, 2007: Optimization of the matrix of weights in the polarimetric algorithm for classification of radar echoes. Preprints, *33rd Conf. on Radar Meteorology*, Cairns, QLD, Australia, Amer. Meteor. Soc., P11B.4. [Available online at http://ams.confex.com/ams/pdfpapers/123123.pdf.]

Ryzhkov, A. V., 2007: The impact of beam broadening on the quality of radar polarimetric data. *J. Atmos. Oceanic Technol.,* **24,** 729–744.

——, and D. S. Zrnić, 1995: Precipitation and attenuation measurements at 10-cm wavelength. *J. Appl. Meteor.,* **34,** 2121–2134.

——, and ——, 1996: Assessment of rainfall measurement that uses specific differential phase. *J. Appl. Meteor.,* **35,** 2080–2090.

——, and ——, 1998: Discrimination between rain and snow with a polarimetric radar. *J. Appl. Meteor.,* **37,** 1228–1240.

——, S. E. Giangrande, V. M. Melnikov, and T. J. Schuur, 2005a: Calibration issues of dual-polarization radar measurements. *J. Atmos. Oceanic Technol.,* **22,** 1778–1785.

——, T. J. Schuur, D. W. Burgess, S. E. Giangrande, and D. S. Zrnić, 2005b: The Joint Polarization Experiment: Polarimetric rainfall measurements and hydrometeor classification. *Bull. Amer. Meteor. Soc.,* **86,** 809–824.

——, and Coauthors, 2007: Comparison of polarimetric algorithms for hydrometeor classification at S and C bands. Analysis of the performance in different climate regions. Preprints, *33rd Conf. on Radar Meteorology*, Cairns, QLD, Australia, Amer. Meteor. Soc., 10.3. [Available online at http://ams.confex.com/ams/pdfpapers/123109.pdf.]

Scharfenberg, K. A., and Coauthors, 2005: The Joint Polarization Experiment: Polarimetric radar in forecasting and warning decision making. *Wea. Forecasting,* **20,** 775–788.

Schuur, T. J., A. V. Ryzhkov, and P. L. Heinselman, 2003: Observations and classification of echoes with the polarimetric WSR-88D radar. NOAA/National Severe Storms Laboratory Rep., 46 pp.

Straka, J. M., 1996: Hydrometeor fields in a supercell storm as deduced from dual-polarization radar. Preprints, *18th Conf. on Severe Local Storms*, San Francisco, CA, Amer. Meteor. Soc., 551–554.

——, and D. S. Zrnić, 1993: An algorithm to deduce hydrometeor types and contents from multiparameter radar data. Preprints, *26th Conf. on Radar Meteorology*, Norman, OK, Amer. Meteor. Soc., 513–516.

——, ——, and A. V. Ryzhkov, 2000: Bulk hydrometeor classification and quantification using polarimetric radar data: Synthesis of relations. *J. Appl. Meteor.,* **39,** 1341–1372.

Vivekanandan, J., D. S. Zrnić, S. Ellis, D. Oye, A. V. Ryzhkov, and J. M. Straka, 1999: Cloud microphysics retrieval using S-band dual-polarization radar measurements. *Bull. Amer. Meteor. Soc.,* **80,** 381–388.

Wakimoto, R. M., and V. N. Bringi, 1988: Dual-polarization observations of microbursts associated with intense convection: The 20 July storm during the MIST project. *Mon. Wea. Rev.,* **116,** 1521–1539.

Zhang, J., C. Langston, and K. Howard, 2008: Brightband identification in vertical profiles of reflectivity from the WSR-88D. *J. Atmos. Oceanic Technol.,* **25,** 1859–1872.

Zrnić, D. S., and A. V. Ryzhkov, 1999: Polarimetry for weather surveillance radars. *Bull. Amer. Meteor. Soc.,* **80,** 389–406.

——, ——, J. M. Straka, Y. Liu, and J. Vivekanandan, 2001: Testing a procedure for the automatic classification of hydrometeor types. *J. Atmos. Oceanic Technol.,* **18,** 892–913.

——, V. M. Melnikov, and A. V. Ryzhkov, 2006: Correlation coefficients between horizontally and vertically polarized returns from ground clutter. *J. Atmos. Oceanic Technol.,* **23,** 381–394.